An Electrohydrodynamic Polarization Micropump for Electronic Cooling

J. Darabi, *Member, IEEE*, M. M. Ohadi, and D. DeVoe, *Member, IEEE*

***Abstract*—This paper presents the design, fabrication, and characterization of an innovative microcooling device for microelectronics applications. The device incorporates an active evaporative cooling surface, a polarization micropump, and temperature sensors into a single chip. The micropump provides the required pumping action to bring the working fluid to the evaporating surface, allowing the effective heat transfer coefficient through a thin-film evaporation/boiling process. The device is based on VLSI microfabrication technology, allowing the electrohydrodynamic (EHD) electrodes to be integrated directly onto the cooling surface. Since the EHD electrodes are fabricated using the same technology as the electronic systems themselves, the proposed microelectronic cooling system in the form of an integrated microchip is very suitable for mass production. The prototype devices demonstrated a maximum cooling capacity of 65 W/cm2 with a corresponding pumping head of 250 Pa. The results of this investigation will assist in the development of future microcooling devices capable of operating at high power levels. [554]**

***Index Terms*—Electrohydrodynamic (EHD), electronic cooling, MEMS, micropump, polarization.**

NOMENCLATURE

A	Area (m^2).
E	Electric field (V/m).
f	Force (N/m^3).
g	Gravitational acceleration (m/s^2).
h	Average heat transfer coefficient ($W/m^2 \cdot K$), height (m).
k	Thermal conductivity ($W/m \cdot K$), dielectric constant.
p	Pressure (N/m^2).
q''	Heat flux (W/m^2).
r	Distance (m).
R	Electric resistance (Ω).
T	Temperature (°C).
ϵ	Permittivity (F/m).
ϵ_0	Permittivity of vacuum (F/m).
ρ	Mass density (kg/m^3).

Subscripts

Pt	Platinum.
Qz	Quartz.
sat	Saturation.
t	Total.
w	Wall.

Manuscript received March 24, 2000; revised August 20, 2000. Subject Editor, O. Tabata.

The authors are with the Department of Mechanical Engineering, University of Maryland, College Park, MD 20742 USA.

Publisher Item Identifier S 1057-7157(01)01586-4.

I. INTRODUCTION

THE miniaturization of electronic components and the rapid increase in power density of advanced microprocessors and electronic components have created a need for improved cooling technologies to achieve high heat-dissipation rates. Some of the next-generation microprocessors and electronic components are projected to dissipate over 1000 W/cm^2. These high heat fluxes cannot be easily dissipated using existing cooling techniques. The need for new technologies capable of dissipating such high heat fluxes with low input power is of critical importance to many industries, particularly for high power density microprocessors and space-based electronic systems. In this paper, we introduce a new technology combining thin-film evaporation and electrohydrodynamic (EHD) polarization pumping for high-efficiency cooling of integrated microsystems.

Among the various microfluidic devices, EHD pumping is a promising option, offering the unique advantage of no moving parts, and thus high reliability. Low cost, very low power consumption, and minimal maintenance are other benefits of the EHD pumping technique. The use of the electrohydrodynamic technique for microscale fluid pumping has been investigated by a number of researchers over the past decade [1]–[7]. In these previous studies, pump designs were based on either ion-drag or induction pumping. In ion-drag and induction pumping, the free charges and dipoles within the liquid are the driving force to pump the liquid. Thus, the power consumption is rather high, resulting in a low pumping efficiency. This paper is based on polarization pumping and incorporates integrated thin-film evaporation/boiling to combine pumping and cooling in a single integrated device. In a polarization pump, the average polarization force over all dipoles induces a body force on the dielectric liquid. Thus, the power required to achieve pumping is very low, leading to higher pumping efficiencies.

The devices developed in this study incorporate active microscale heat transfer surfaces, a micropump, and temperature sensors in a single package that may be directly attached to a heat source. This design offers several engineering advantages. The electric field is applied directly to the heat transfer surface in order to minimize voltage requirements, reduce thermal resistance, and maximize the effective heat transfer coefficient. The EHD micropump provides the pressure head required to drive the working fluid through the evaporation loop.

Traditional macroscale EHD pumping mechanisms require significant voltages in order to reach sufficient electric field strengths (in the range of 10–20 kV [8]). In contrast, microscale EHD pump-based cooling has the following advantages.

1) Microscale electrode gaps can allow the system to operate using the same low dc voltages as the electronics them-

1057–7157/01$10.00 © 2001 IEEE

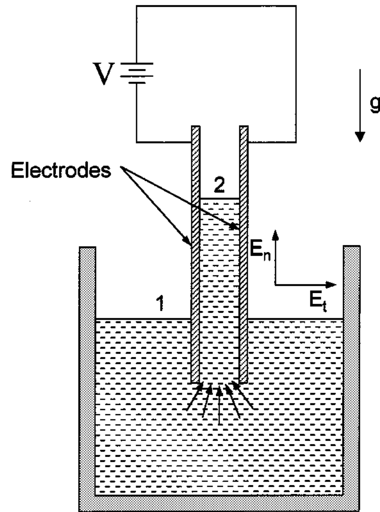

Fig. 1. A pair of parallel plates dipped into a dielectric liquid.

selves. For example, the voltage requirement is expected to be less than 15 V for an electrode gap of 5 μm.

2) EHD polarization micropump employs dc electrical currents on the order of microamps (in the range of 10–50 V). Therefore, the total power requirement to operate the device can be negligible.
3) The manufacturing methods are applicable to high-volume batch fabrication, making this technology cost effective.
4) The low-voltage dc operation of the EHD micropump will not create electromagnetic interference with electronic systems.

II. Theoretical Background

The mechanism by which liquids rise between a pair of parallel electrodes when subjected to an electric field can be understood from the following [9]. Consider the simple case shown in Fig. 1 in which a pair of parallel electrodes is dipped into a dielectric liquid. If a potential difference V is applied between the electrodes, the dielectric liquid rises between the electrodes due to a net electrostatic force acting on dipoles in the liquid. This force is arises from the local electric field gradient at the end of the electrode pair. In a polarized medium, each individual dipole is subjected to an electric force and transmits this force to the neutral molecules. This is either because the dipoles are tied to a lattice structure or through a collision mechanism. A dipole can be represented by a pair of oppositely signed charges of $(+q)$ and $(-q)$ separated by a distance $\vec{r}$. The net force on each dipole can be given by

$$\vec{f} = \vec{p} \cdot \nabla \vec{E} \tag{1}$$

where $\vec{p} = q \cdot \vec{r}$ is the dipole moment. Melcher [9] assumed that the dipoles were subject to an average or macroscopic electric field. This assumption ignores the distortion of the electric field at one dipole because of neighboring dipoles. The total polarization force can be found by averaging these polarization forces over all dipoles within the dielectric medium. One simple approach would be to multiply the net force on each dipole by the total number of the dipoles per unit volume n. Defining the polarization density as $\vec{P} = n\vec{p}$, the polarization force density can be written as

$$\vec{F} = \vec{P} \cdot \nabla \vec{E}. \tag{2}$$

The relation between the polarization force and electric field $\vec{E}$ can be written as [10]

$$\vec{P} = \varepsilon_0 (k-1)\vec{E}. \tag{3}$$

Substituting (3) into (2) and assuming constant permittivity, the polarization force density becomes

$$\vec{F} = \nabla \left(\frac{\varepsilon_0}{2}(k-1)\vec{E} \cdot \vec{E} \right). \tag{4}$$

The polarization force given by (4) does not take into account the interaction between dipoles. Moreover, it is an average over a spectrum of dipole moments. If p is the pressure in the liquid, the mechanical volume force $-\nabla p$, which is set up as a result of the pressure gradient, is equal and opposite to $\vec{F}$. In other words

$$\vec{F} = \nabla p. \tag{5}$$

By a comparison of (4) and (5), we obtain

$$p_1 - p_2 = \frac{\varepsilon_0 (k-1)}{2} E^2. \tag{6}$$

This equation gives only the net difference in pressure from level 1 to level 2, indicated in Fig. 1. It does not describe the detailed pressure behavior in the liquid. The height to which the liquid rises against the gravity between the electrodes may be expressed as

$$h = \frac{\varepsilon_0 (k-1)}{2\rho g} E^2 \tag{7}$$

where ρ is the density of the liquid and g is the acceleration of gravity.

The force that pushes the liquid up against the gravity is exerted at the lower edges of the plates, where the field is inhomogeneous and the electric field density varies rapidly. This can be explained by the fact that the energy of the dipoles in a field-free space is higher than their energy in the electric field. Thus, the dipoles in the field-free region are pulled into the region of higher electric field between the plates, where the potential energy is minimum. It should be noted that the polarization forces have been known for quite some time [9]. However, this study is the first of its kind to use the polarization force to achieve pumping for high heat flux electronic cooling applications.

It has been demonstrated that the electrical control of the interfacial tension at the liquid/solid interface could decrease the surface tension of an electrolytic fluid, leading to liquid pumping within a set of closed microchannels or capillaries [11]. The phenomenon is known as electrowetting. This effect, however, was not considered here because the pumping mechanism described in this paper only works with dielectric fluids.

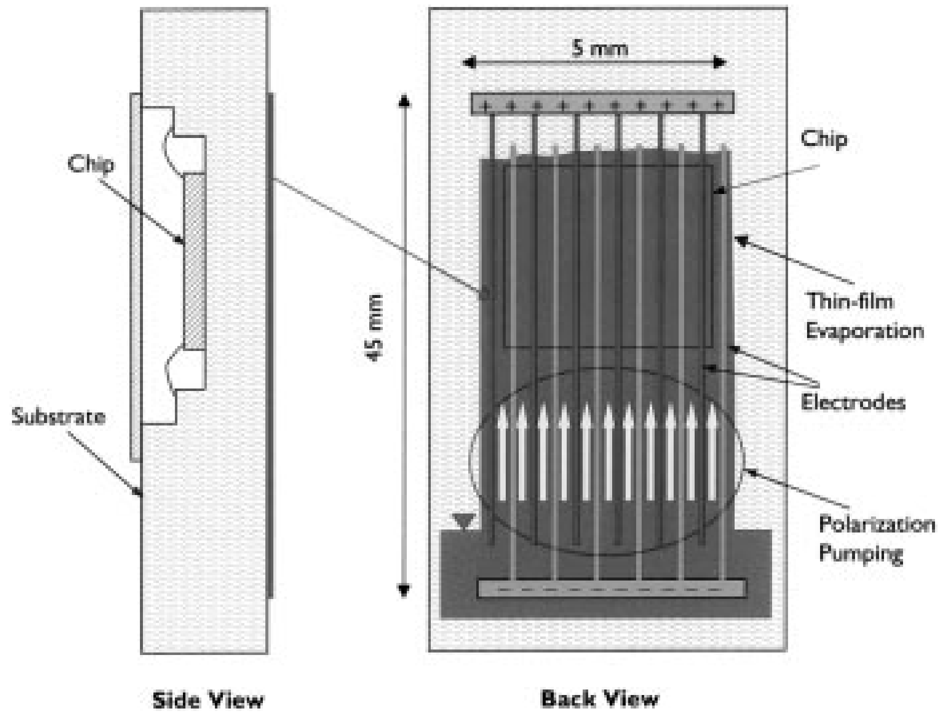

Fig. 2. Conceptual illustration of the device (not to scale).

Also, in this case, the electrodes are planer and there are no capillaries or microchannels.

III. Description of the Device

Based on the many advantages of the polarization micropump, several design concepts were implemented to explore the potential of such a device. A conceptual illustration of the device is shown in Fig. 2. Note that this drawing is not to scale. The experimental system described in this paper measures 5 mm $\times$ 50 mm. To simulate the heat generated from a chip in operation, an array of platinum heaters is incorporated onto the substrate. The dimension of heater array is 5 mm $\times$ 5 mm.

A. Design

This design suffered from problems with the insulating layer between the electrodes and substrat, connecting the power leads, and concerns about heat conduction through the substrate. Another potential problem was microscopic pin holes in the SiO_2 layer. Microscopic pinholes in an oxide layer may cause a short circuit between the electrodes and the substrate.

The second design employed a double-sided polished sapphire wafer as a substrate, with the EHD electrodes on one side and the microheaters on the other side. This design avoids the issue of oxide breakdown in the SOI design. However, heat conduction through the substrate was still a concern. A modification of this design led to the third (present) design, which used a single side polished quartz wafer as a substrate, and housed both the micro heaters and electrodes on the front side. Table I compares the relevant properties of the three different substrates that were considered.

TABLE I
THERMOPHYSICAL PROPERTIES OF DIFFERENT SUBSTRATE MATERIALS

Material	Thermal Conductivity (W/m.K)	Resistivity (Ohm.cm)	Dielectric Constant
Silicon	80 - 150	10^{18}	Conductive
Sapphire	35 - 40	10^{14}	7.5-11.5
Quartz	1.46	23×10^4	3.8

The microheaters are formed by serpentine platinum lines with widths of 50 and 100 μm. Each heater array consists of four or eight microheaters depending on the width of the platinum heater lines. The platinum heater lines are either 50 or 100 μm wide, with 10- and 20-μm spaces in between the lines. Each individual heater is approximately 3.1 mm and 6.2 mm^2 for the 50- and 100-μm heater lines, respectively. Fig. 3 shows the schematic diagram of the device. Note that this drawing is not to scale.

The electrical resistances of the heaters are about 190 and 720 Ω at room temperature for the 50- and 100-μm heater lines, respectively. Current passing through this array of heaters causes electrical power to be dissipated as thermal energy, simulating the chip to be cooled. The change in the platinum's resistance with temperature allows the surface temperature of the heater to be determined by measuring the resistance of the heater. In determining the heater resistance, two factors were considered. The total resistance should be high enough so that the thermal resistance in the connections will not cause a significant error in the temperature measurements. On the other hand, the resistance must be low enough that common low-voltage power supplies can be used to power the heaters.

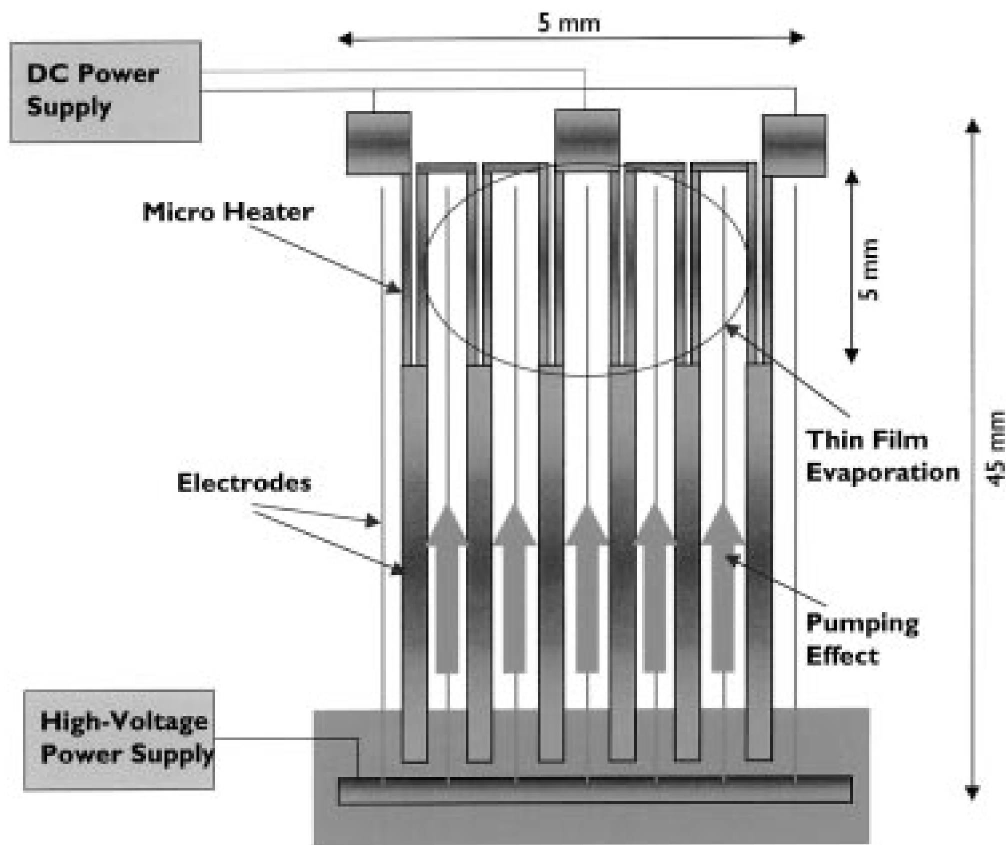

Fig. 3. Schematic diagram of the device (not to scale).

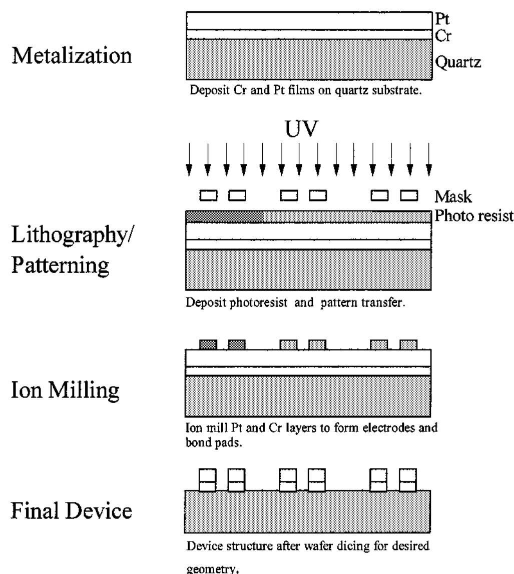

Fig. 4. Simplified fabrication flow of the electrode.

B. Fabrication

The simplified microfabrication process is shown in Fig. 4. The fabrication sequence begins with wafer premetallization cleaning, followed by a deposition of 300 °A chromium and 2500 °A platinum using an e-beam evaporator. Next, the Cr/Pt film was patterned using ion milling to define the heater and EHD micropump electrodes, followed by dicing of the quartz wafer into individual devices. Following microfabrication, packaging was performed. The devices were mounted on the backside of ceramic dual in-line pin (DIP) packages using high-temperature transparent epoxy adhesive. The dimensions of the ceramic DIP packages were 15 mm $\times$ 60 mm. Once the device was mounted on the DIP package, electrical connections were made between the electrodes, the heater array, and the DIP package. A photograph of a packaged device is shown in Fig. 5. Since the number of bond pads on each device was on the order of ten or less, wire bonding was performed between the bond pads and the root of the DIP pins. Gold wire was used for the wire bonding. The external wires were also soldered to the outside of the DIP pins.

C. Calibration of the Heaters

Heating power was supplied to the device by an array of platinum heaters. In this design, the wall temperature was calculated by measuring the platinum heater resistance. The heaters were first calibrated, and the relationship between the temperature and the resistance was then established. This was accomplished by heating a refrigerated bath/circulator to the desired calibration temperature and placing the heater in the bath. This system provided reliable temperature control with a temperature stability of ± 0.03 °C. First, the bath was allowed to reach steady state at a set temperature. Once the heater came to an equilibrium with the bath, a threshold voltage of 1 V (equivalent to a power level of 5 mW) was applied to the heater. A precision power supply was used to supply a stable voltage with a fluctuation on the order of μV. Next, the data acquisition system was

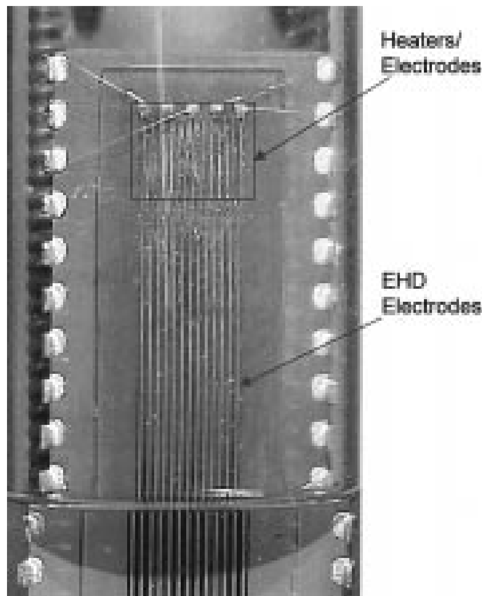

Fig. 5. Photograph of the packaged device.

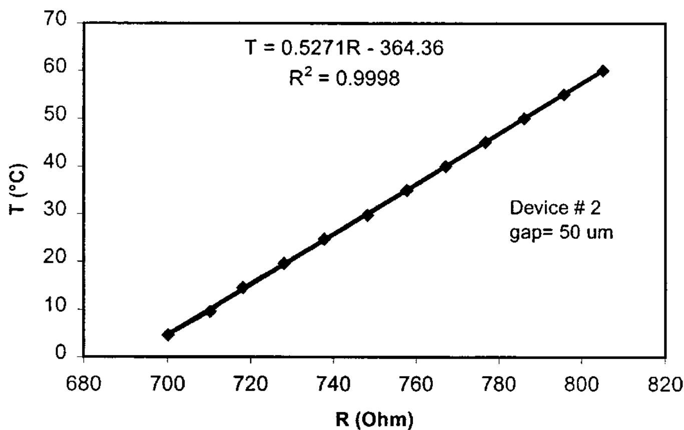

Fig. 6. Typical results of temperature calibration (device 2).

switched on, and the current and voltage were recorded over a time span of 30 min, averaged and recorded to a file. The resistance was determined from the measured voltage and current data. These preceding steps were repeated for the same temperature for other heaters in the array. These procedures were repeated for other calibration temperatures, and the relationship between temperature and resistance was obtained. The heater was calibrated at 12 temperatures, and a linear fit was used to obtain the relationship between the resistance and temperature of the heater. Fig. 6 shows a typical calibration result and a linear fit through the data points.

IV. Experimental Apparatus

A photograph of the setup is shown in Fig. 7. The setup consists of a glass test chamber, a refrigerated bath/circulator, a test device, a data acquisition system, and other measurement devices. A brief description of each component follows.

The test chamber consists of two brass flanges, a glass cylinder, a condenser, a brass rod, and a base plate. The glass cylinder is 150 mm in length with a 19-mm inside diameter and a wall thickness of 3.4 mm. It was designed to sustain up to 1.725-MPa pressure. Flanges at both the top and the bottom of the chamber were sealed using O-rings. To fix the test device in place inside the test chamber, a slot was made in a Teflon rod and fixed on the bottom flange. The test device can be easily inserted or removed from this Teflon rod. Three swagelock connections were made into a brass rod to provide connections between the electric heater wires, the RTD wires, and the high-voltage power supply. To seal the wire connections, ten small holes were made in a 6.35-mm Teflon rod and sealed by a swagelock connection. Besides providing a primary support for the chamber, the top flange serves as the base for a tube-in-tube condenser. The chilled water flows in the annulus and condenses the refrigerant vapor in the tube side. A pressure transducer is installed on the top flange to measure the system pressure. In addition, a valve is also installed on the top flange for charging and discharging the working fluid. For safety, a relief valve is mounted on the top flange.

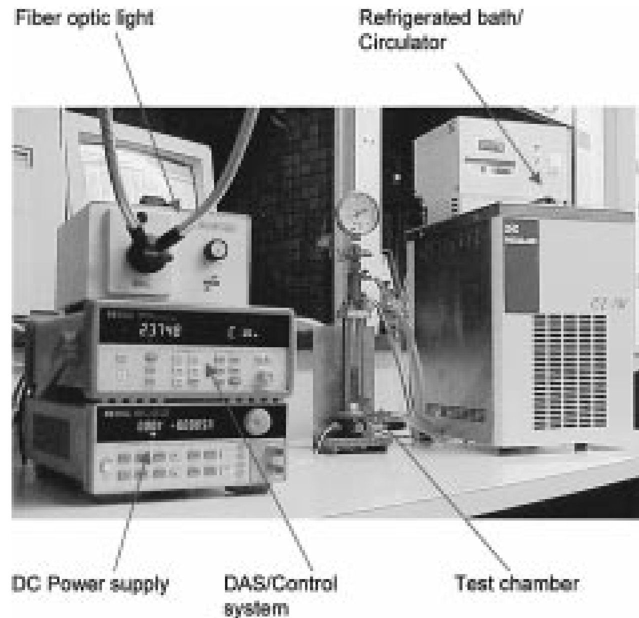

Fig. 7. Photograph of the experimental setup.

A 300-W NESLAB refrigerated bath/circulator was used to provide the cooling requirement and to calibrate an array of microscale heaters. This system provides reliable temperature control with a temperature stability of ± 0.03 °C. The bath temperature can be adjusted from -12 °C to $+130$ °C. Other features include a microprocessor controller, which offers multistep programming and remote sensing capabilities and an adjustable high-temperature safety cutoff. The amount of mass flow rate of chilled water circulating in the test section was evaluated by a computer, based on the preset chamber pressure. The output signal was then sent to the stepper motor utilizing an analog-to-digital card, and the desired adjustment in the chilled water flow rate was made.

A Hewlett-Packard (HP) data acquisition/switch unit Model 34 970A was used to monitor, control, and acquire data. The data acquisition system consisted of a personal computer, a data acquisition/switch unit, an HP 34901A 20-channel multiplexer,

an HP 34903A 20-channel actuator/general-purpose switch, and an HP Benchlink data logger software.

A variable HP 6614C System dc power supply with output ranges 0–100 V and 0–0.5 A was used to provide the electric power to an array of microscale platinum heaters. This dc power supply offers high performance with low-output noise and output current measurement capability in the microampere range. The 6614C power supply also provides high-speed programming with under 4 ms response time.

V. Experimental Procedure

A typical experimental run started by switching on the refrigerated bath/circulator. The circulator was then set to the desired temperature, which was approximately 25 °C. The bath temperature was monitored, and when it reached steady state, the EHD voltage was switched on and the positive electrodes were supplied with a dc voltage of 0–300 V. Next, the heater power supply was switched on and set at a fixed power. The heater temperature was monitored and allowed to reach steady state. The data acquisition was then switched on and data recorded over a time span of 30 min and recorded to a file for post-processing. The process was repeated for multiple increments in heater power, and data recording was continued until partial dryout occurred at some part of the heater.

VI. Data Reduction

The heat flux was calculated from the voltage and the current across the heater. To account for substrate conduction, the following methodology was used to determine the magnitude of the actual heat flux.

One-dimensional heat transfer analysis was performed to find the heat losses from the backside of the device. Heat conduction through the electrodes was neglected in this analysis. Fig. 8 shows the different layers of the device, which can be considered as composite walls and its equivalent thermal circuit. Heat transfer occurs from the hot surface by conduction through the walls and by convection from the other surface of the wall to the vapor at $T_{\rm sat}$. Since the heater temperature $T_{\rm Pt}$ and the saturation temperature are known, the one-dimensional heat transfer rate for this system can be easily found from

$$q_{\rm loss} = \frac{T_{\rm Pt} - T_{\rm sat}}{R_t} \tag{8}$$

where R_t is the total thermal resistance and given by

$$R_t = \frac{L_{QZ}}{k_{QZ}A} + \frac{L_{\rm epoxy}}{k_{\rm epoxy}A} + \frac{L_{\rm ceramic}}{k_{\rm ceramic}A} + \frac{1}{hA}. \tag{9}$$

The average surface temperature was determined from the heater resistance. The saturation temperature was measured by two 100-Ω platinum RTDs. One of the RTDs was located in the pool, and the other one was in the vapor region. The measured temperature difference between the two RTDs was less than 0.05 °C. The accuracy of the RTDs was ±0.08 °C.

The average convection coefficient of the vapor was assumed to be 10 $W/m^2 \cdot K$. Table II provides the thermal conductivity and thickness of the different materials. The heat loss through the substrate was calculated using the above procedure and was

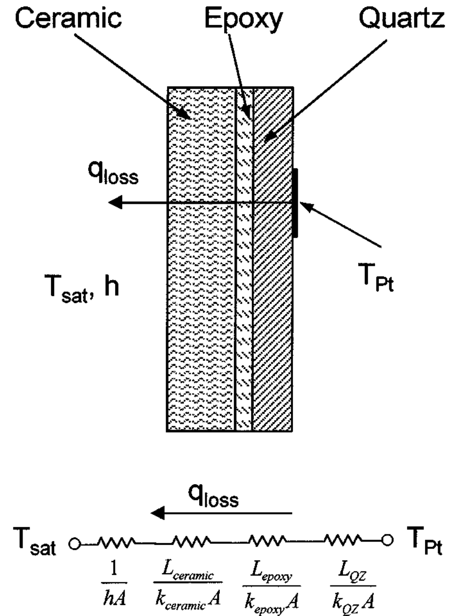

Fig. 8. Different layers of the device and its equivalent thermal circuit.

TABLE II
Thermal Conductivity and Thickness of Different Materials

Material	Thermal Conductivity (W/m.K)	Wall Thickness (mm)
Quartz	1.46	0.5
Epoxy	1.5	0.2
Ceramic	18	2.2

found to be less than 1% of the total power to the heater. The heat loss through the substrate was then subtracted from the total heat transfer rate to obtain the net heat flux to the evaporative surface.

The average heat transfer coefficient h was found from

$$h = \frac{q''}{T_w - T_{\rm sat}} \tag{10}$$

where q'' is the net heat flux and T_w and $T_{\rm sat}$ are the mean wall and saturation temperatures, respectively.

VII. Uncertainty Analysis

The uncertainties in the heat flux and the average heat transfer coefficient were determined using the propagation of error suggested by [12] and [13]. The uncertainty in heat flux results from the uncertainties in total power to the heater and heat losses through the substrate. The uncertainty in the total power to the heater arises from uncertainty in measured voltage and current across the heaters. Since heat losses through the substrate represent less than 1% of the total heat transfer, there is a relatively small uncertainty in the net heat flux.

The uncertainty in heater temperature results from the uncertainties in the measurements of current and voltage to obtain the resistance, temperature-resistance calibration curve, and the bath temperature. The final uncertainty in heater temperature was estimated to be ±0.2 °C. The uncertainty in calibrating bath

TABLE III
THERMOPHYSICAL AND ELECTRICAL PROPERTIES OF R-134a AT 25 °C (REFPROP 6.0 [14])

Property	Value
Liquid density (kg/m^3)	1207
Liquid thermal conductivity (W/m.K)	0.08785
Liquid viscosity (N.s/m^2)	0.000247
Latent heat (kJ/kg)	176.557
ε_l (PF/m), Bryan [15]	90.0
ε_v (PF/m), Bryan [15]	11.5

temperature was smaller compared to that of the heater. Uncertainty in the saturation temperature was ±0.08 °C.

Flow visualization using a video camera was performed to determine the rise of liquid between the electrodes due to the action of the EHD polarization pump. The height of the device was calibrated using a pair of calipers. The height to which the liquid rises between the electrodes was then determined by enlarging snapshots of the video and comparing it with the calibrated device. The uncertainty in the height was estimated to be ±0.5 mm.

VIII. RESULTS AND DISCUSSION

Several microcooling devices are fabricated and tested to investigate the feasibility of employing EHD pumping/thin-film evaporation for cooling of high-power electronics. Each device incorporates an active heat transfer surface, a micropump, and temperature measurement sensors into a single chip. Microfabrication technology allows the EHD electrodes to be integrated directly on the heat transfer surface, facilitating the manufacturing processes. Also, applying the electric field directly to the heat transfer surface can provide better control over liquid film thickness for optimal thin-film evaporation. The micropump provides the required pumping action to bring the working fluid to the heat transfer surface.

All the experiments were performed at a saturation temperature of 25 °C to minimize heat losses or gains to or from the surroundings. The working fluid was R-134a. Refrigerant R-134a is a commercially available hydrofluorocarbon refrigerant with zero ozone depletion potential. Table III lists the thermophysical and electrical properties of R-134a. The heat flux, heater temperature, and heat transfer coefficient were averaged over the heaters. Two different devices with the electrode spacing of 50 and 100 μm were fabricated and tested. The specifications of these devices are shown in Table IV.

Unlike conventional EHD cooling systems, the MEMS-based EHD system can be operated from the same low dc voltages as the electronics themselves, eliminating the need for a high-voltage power supply. In the current design, the polarization voltage was around 150 V for a 50-μm electrode gap. In future designs, this voltage will be further reduced to that of the conventional electronics by scaling down the devices and reducing the electrode gap sizes. For example, by reducing the electrode gap to 3–5 μm, the required voltage is expected to be 9–15 V.

TABLE IV
SPECIFICATIONS OF THE TESTED DEVICES

Device	# 1	# 2
Electrode spacing (μm)	100	50
Width of the electrode lines (μm)	20	10
Dimensions of the heater array (mm × mm)	5 × 5	5 × 5
Number of heaters in the array	4	8
Width of the platinum heater lines (μm)	100	50
Space between the heater lines (μm)	20	10
Resistance at room temperature (Ω)	190	720

The boundaries between the heat transfer modes were established from visual observation of the device using a transparent glass tube in a series of experiments. The possible heat transfer modes observed are discussed in the following.

At very low heat fluxes, the heat transfer mode was found to be in the convection mode with most of the liquid flowing upward along the plate, overflowing, and returning to the pool of liquid. This was mainly due to the low heat transfer rate.

As the heat flux was increased, evaporation was observed on the top portion of the plate. However, convection still dominated. Enhanced convection was assumed to occur due to electroconvection caused by the electric field. Electroconvction is driven by interaction of an external electric field with an inhomogeneous space charge density. When a dc voltage is applied to the electrodes, pairs of alternating vortices are set in the flow. With increasing voltage, these vortices become unstable leading to electrically induced secondary motions and the resulting heat transfer enhancement.

For intermediate heat fluxes, the heat transfer mode was governed solely by evaporation and a relatively smooth interface was observed. As the heat flux was further increased, the boiling mode of heat transfer was observed in the lower portion of the evaporating surface. This heat transfer mode seemed to be unstable, and oscillation between boiling and evaporation was observed.

At high power levels, the heat transfer was dominated by boiling, and boiling was observed on almost the entire area of the heat transfer surface. The flow for these conditions was highly agitated, resulting in a highly irregular interface. The liquid supply to the heaters was occasionally cut off by bubbles generated on the surface.

At very high heat flux levels, boiling was the only mode of heat transfer, and dryout was observed at a large region of the surface on the top portion. The dryout occurred when the evaporation rate was higher than the rate of liquid supply by the EHD pump.

Fig. 9 shows the pumping head results. The results are also compared with the theoretical calculations in (6), showing that as the electrode gap decreases, the results approach those of the analysis, suggesting that further miniaturization may increase the pumping efficiency. Visual observation of the device showed that capillary effects did not contribute to the rise of the liquid between the electrodes. This is believed to be due to the rather

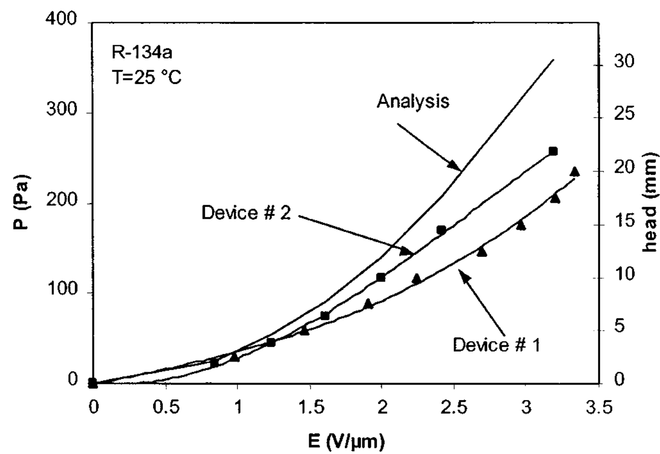

Fig. 9. EHD pumping results.

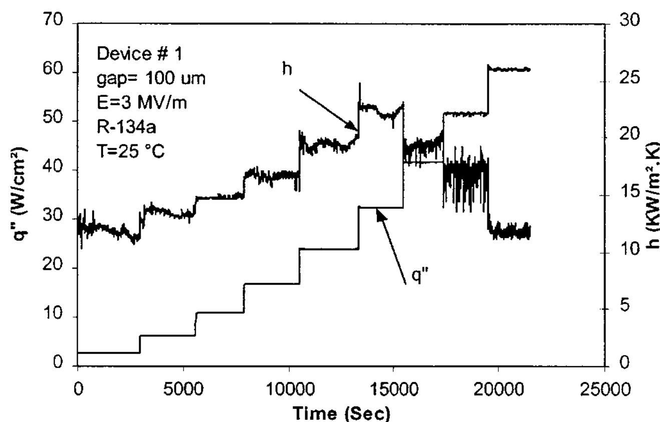

Fig. 10. Spatially averaged time-resolved results for device 1.

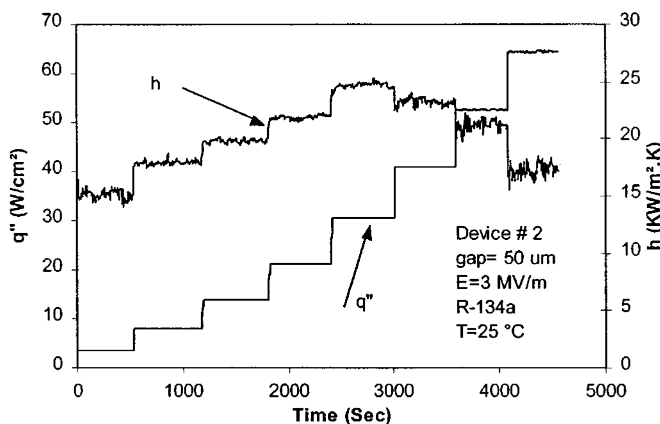

Fig. 11. Spatially averaged time-resolved results for device 2.

large ratio of the distance between the electrodes to the thickness of the electrodes, which was greater than 200.

Spatially averaged, time-resolved heat transfer coefficient results are shown in Figs. 10 and 11. Typically, a moderate increase in the heat transfer coefficient is seen with heat flux, followed by a peak and a moderate drop. It is believed that the peak represents a case when a thin film covers the entire surface and heat transfer takes place effectively by evaporation. Visual observation confirmed this postulate. Similar behavior was observed for both devices. Heat-transfer results for the device with

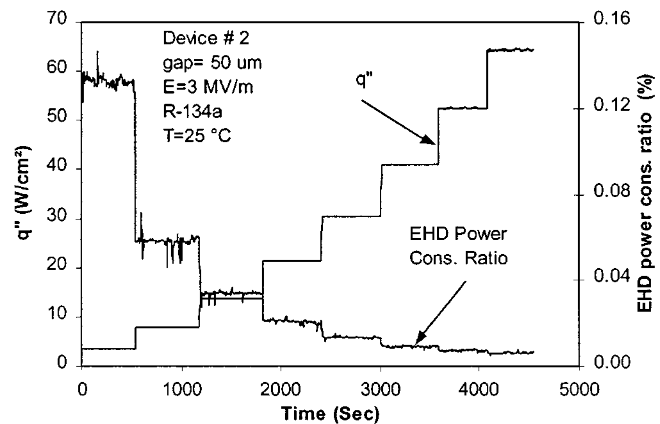

Fig. 12. EHD power-consumption ratio for device 2.

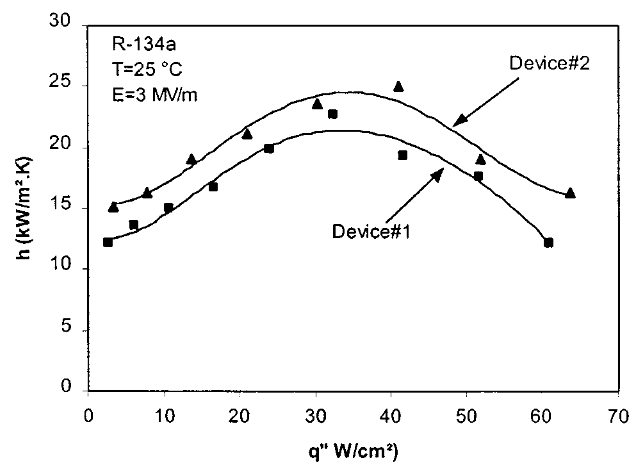

Fig. 13. Spatially averaged time-averaged results.

an electrode spacing of 50 μm were found to be slightly higher than those of 100-μm electrode spacing. This is perhaps due to a more uniform film distribution at a smaller electrode gap. A rather large fluctuation in the heat-transfer coefficient was found at high heat fluxes. This was due to a partial dryout and rather vigorous bubble formation and departure at high power levels, which occasionally cut off the liquid supply to the heaters.

Fig. 12 shows selected EHD power-consumption results. The EHD power-consumption ratio is defined to quantify the ratio of electrical power consumption by the electrodes over the total power input to the device. For the range of the power levels of interest, the EHD power consumption is less than 0.02% of the total power input to the device. In general, the current decreases with heat flux, because as heat flux increases, the amount of vapor in the system also increases. Since the electrical conductivity of the vapor is less than liquid, the current decreases as the vapor fraction increases. However, the sharp drop in the EHD power consumption ratio is not due to the aforementioned effect. It is due to the fact the even if the EHD power consumption (numerator) remains constant, since the total power input to the device (denominator) increases with increasing heat flux, this ratio decreases as the heat flux increases.

Fig. 13 shows the spatially averaged time-averaged heat transfer data as a function of heat flux. Results indicate that the heat transfer coefficient initially increases with heat flux,

reaches a maximum, and then decreases. At low heat-flux levels, the heat transfer is mainly governed by electroconvection caused by the electric field. As heat flux increases, a transition from convection to evaporation occurs, resulting in a higher heat transfer coefficient. Further increase in heat flux causes a partial dryout and interruption of the liquid supply to the heaters, leading to a sharp drop in heat transfer coefficients.

IX. Conclusions

An experimental investigation was conducted to study the feasibility of combining microfabrication technology with the EHD technique for high heat-flux electronic cooling applications. The results of the experiments successfully validated the concept and a maximum cooling capacity of 65 W/cm^2 was achieved using R-134a as the working fluid. The experimental results also indicated a pumping head of 250 Pa at an applied voltage of 150 V.

A unique feature of this novel cooling device is that it integrates an active evaporative surface and an EHD micropump into a single chip, greatly facilitating the manufacturing process, increasing the cooling capacity, and improving the thermal management of future high-power density electronic devices. Unlike conventional EHD systems, the microfabricated EHD system can be operated from the same low dc voltages as the electronics themselves, eliminating the need for a high-voltage power supply. In the current design, the polarization voltage was around 150 V for a 50-μm electrode gap. This voltage can be further reduced to that of electronics by scaling down the devices and reducing the electrode gap to 2–5 μm.

This micropump has high commercialization potential and may pave the way for practical utilization of thin-film evaporation in many applications. Utilizing thin-film evaporation, which is one of the most effective means of heat removal, the device can substantially increase the cooling capacity and lead to substantial weight/volume reduction in many thermal management systems. The results of this investigation will assist in the development of microcooling devices capable of operating at higher power levels. This technology also shows great promise for other micropumping applications due to the low voltages and high efficiency inherent in the EHD polarization mechanism.

References

[1] S. F. Bart, L. S. Tavrow, M. Mehregany, and J. H. Lang, "Microfabricated electrohydrodynamic pumps," *Sensors Actuators A*, vol. 21, no. 1, pp. 193–197, 1990.

[2] A. Richter, A. Plettner, K. A. Hofmann, and H. Sandmaier, "A micromachined electrohydrodynamic (EHD) pump," *Sensors Actuators*, vol. 29, no. 2, pp. 159–168, 1991.

[3] G. Fuhr, R. Hagedorn, T. Muller, and W. Benecke, "Microfabricated electrohydrodynamic (EHD) pumps for liquids of higher conductivity," *J. Microelectromech. Syst.*, vol. 1, no. 3, pp. 141–146, 1992.

[4] G. Fuhr, T. Schnelle, and B. Wagner, "Traveling wave-driven microfabricated electrohydrodynamic pumps for liquids," *J. Micromech. Microeng.*, vol. 4, no. 4, pp. 217–226, 1994.

[5] Y. K. Youn and Y. K. Kim, "Micro pumps using electrostatic forces," *Trans. Korean Inst. Elect. Eng.*, vol. 43, no. 12, pp. 2010–2019, 1994.

[6] J. W. Choi and Y. K. Kim, "Micro electrohydrodynamic pump driven by traveling electric fields," in *Proc. IEEE IAS*, vol. 2, 1995, pp. 1480–1484.

[7] S. H. Ahn and Y. K. Kim, "Fabrication and experiment of planar micro ion-drag pump," in *Proc. Transducers'97*, 1997, pp. 373–376.

[8] J. E. Bryan and J. Seyed-Yagoobi, "An experimental investigation of ion-drag pump in a vertical and axisymmetric configuration," *IEEE Trans. Ind. Applicat.*, vol. 28, no. 2, pp. 310–316, 1992.

[9] J. R. Melcher, *Continuum Electromechanics*. Cambridge, MA: MIT Press, 1981.

[10] W. K. H. Panofsky and M. Phillips, *Classical Electricity and Magnetism*. Reading, MA: Addison-Wesley, 1962.

[11] H. Matsumoto and J. E. Colgate, "Preliminary investigation of micropumping based on electrical control of interfacial tension," in *Proc. IEEE MEMS'90*, Feb. 1990, pp. 105–110.

[12] S. J. Kline and F. A. McClinock, "Describing uncertainties in single sample experiments," *Mech. Eng.*, vol. 75, pp. 3–8, Jan. 1953.

[13] R. J. Moffat, "Describing the uncertainties in experimental results," *ASME J. Fluid Eng.*, vol. 107, pp. 250–260, 1988.

[14] National Institute of Standards and Technology, Gaithersburg, MD, REFPROP 6.0, Thermodynamic and Transport Properties of Refrigerants and Refrigerant Mixtures Database.

[15] J. E. Bryan, "Fundamental study of electrohydrodynamic-enhanced boiling heat transfer," Ph.D. dissertation, Texas A&M University, College Station, 1998.

J. Darabi (S'82–M'84) received the Ph.D. degree in mechanical engineering from the University of Maryland, College Park, in 1999.

Currently, he is a Member of Research Faculty at the University of Maryland. His active research interests are in the areas of microelectromechanical systems, electronic cooling, and micropumps. While perusing his graduate studies at the University of Maryland, he pioneered several novel micropumps and microcooling devices for high heat-flux electronic cooling. He is currently active in the development of micropumps for cooling spatially separate electronic components at cryogenic temperatures and micro heat exchangers.

Dr. Darabi is a member of ASME and ASHRAE. He received the Homer Addams Award (1999), the University of Maryland Outstanding Student Service Award (1999), and the ASHRAE Grant-in-Aid Fellowship (1995–1996 and 1998–1999).

M. M. Ohadi is a Professor of mechanical engineering at the University of Maryland, College Park. He has close to 20 years of industrial and academic experience in the areas of heat transfer, fluid flow, thermal energy conversion, and electrohydrodynamics. He was formerly Chair of the ASME Process Industry Division. He is the Associate Editor of the *Journal of Enhanced Heat Transfer* and the *ASME Journal of Manufacturing Science and Technology*. Since 1985, his research has focused on active and hybrid augmentation of single-phase and phase-change heat transfer. His current funded research includes projects on air-side heat transfer enhancement, external and in-tube boiling and condensation, melting and freezing, and study of thermal/fluid characteristics of alternative refrigerants such as CO2 and ammonia. He

Prof. Ohadi has received several awards, including the ASME/JSME Distinguished Contribution Award (1999), the Japanese STA Fellowship Award (1998), the SAE Ralph R. Teetor Distinguished Faculty Award (1988), and the State of Michigan MAGB Award (1989). He is an active member of ASHRAE and currently is Vice Chair of the committee on refrigerant-to-air heat exchangers. His work in enhanced heat transfer has appeared in more than 120 technical publications and is internationally recognized.

D. DeVoe (S'93–M'97) received the Ph.D. degree in mechanical engineering from the University of California, Berkeley.

In 1997, he joined the Department of Mechanical Engineering at the University of Maryland, where he holds a joint appointment with the Institute for Systems Research and is an Assistant Professor of mechanical engineering. He is a Founding Director of the Center for Micro Engineering at the University of Maryland, where his interests include novel silicon microfabrication technologies, bio-MEMS, and thin-film piezoelectric microsystems.

Dr. DeVoe received the 1999 NSF Presidential Early Career Award for his work in micromechanism technology. He is currently serving the MEMS technical community in several ways. He initiated and is serving as Chair of the Society of Experimental Mechanics 2000–2001 Microsystems Conference. He also serves on the executive committee for the MEMS Subdivision of the American Society of Mechanical Engineers and as a committee member for MEMS-related conferences including ASME, AVS, and SPIE.